Available online at www.sciencedirect.com
SCIENCE DIRECT®
Remote Sensing of Environment 87 (2003) 295–309
Remote Sensing of Environment
www.elsevier.com/locate/rse

The effects of vegetation phenology on endmember selection and species mapping in southern California chaparral

Philip E. Dennison*, Dar A. Roberts

Department of Geography, University of California Santa Barbara, EH3611, Santa Barbara, CA 93106, USA

Received 19 March 2003; received in revised form 29 May 2003; accepted 4 July 2003

Abstract

Image classification typically utilizes single-date imagery and does not take into account seasonal variation in the spectral characteristics and separability of image spectra. While global vegetation classifications have relied on seasonal changes in multitemporal data, seasonal vegetation dynamics have seldom been explored at higher spatial and spectral resolutions. In particular, investigations of vegetation phenology in the hyperspectral domain have been limited. This paper uses endmember average root mean square error (EAR), a method for selecting endmembers for multiple endmember spectral mixture analysis (MESMA), to explore temporal changes in the spectral characteristics of the selected endmembers. The images modeled by these endmembers demonstrate temporal changes in the confusion between vegetation species in southern California chaparral.

Endmembers were selected from five Airborne Visible Infrared Imaging Spectrometer (AVIRIS) images of the area surrounding Santa Barbara, CA, USA. The selected endmembers demonstrated spectral changes that were consistent with an increase in nonphotosynthetic vegetation (NPV) as soil water balance decreased. Polygon level modeling accuracies for soil water surplus images ranged between 59% and 90%, while accuracies for soil water deficit images ranged between 52% and 81%. Variation in NPV content in the water deficit images resulted in increased confusion between chaparral species. Increasing the number of endmembers used to model each land cover class significantly increased accuracy in the water deficit images. Seasonal variations in the spectral response of chaparral are important for determining the separability of chaparral species.

Keywords: Vegetation phenology; Spectra mixture analysis; endmember selection; Vegetation mapping; Hyperspectral time series

1. Introduction

Vegetation phenology can provide a useful signal for classifying vegetated land cover, but phenology is also a source of confusion for change detection. Changes in vegetation spectral response caused by phenology can conceal longer term changes in the landscape (Hobbs, 1989; Lambin, 1996). Multitemporal data that captures these spectral differences can improve separability of vegetation types over classifications based on single-date imagery (DeFries, Hansen, & Townshend, 1995). Global-scale land cover classifications have utilized differences in vegetation phenology derived from multitemporal data to map the distribution of ecoregions (DeFries & Townshend, 1994; Loveland et al., 2000). While global-scale monitoring of phenology has been successful, hyperspectral analyses of seasonal changes in vegetation have been limited due to the restricted abilities of aerial platforms to repeatedly sample large areas (Elvidge & Portigal, 1990; Garcia & Ustin, 2001; Merton, 1998; Roberts, Green, & Adams, 1997). The spectral detail provided by hyperspectral data allows classification of vegetation species (Dennison & Roberts, 2003) and monitoring of the nonphotosynthetic vegetation (NPV) component of vegetation canopies (Roberts, Smith, & Adams, 1993). NPV fraction is an important indicator of wildfire fuel condition (Roberts et al., 2003).

Previous studies incorporating hyperspectral time series have utilized data from the Jasper Ridge Biological Preserve, California, USA. Elvidge and Portigal (1990) found dramatic seasonal spectral changes in annual grasslands and smaller spectral changes in evergreen vegetation in a three-date time series of Airborne Visible Infrared Imaging Spectrometer (AVIRIS) data. Roberts et al. (1997) modeled liquid water absorption, green vegetation fraction, and non-

*Corresponding author. Tel.: +1-805-893-4434; fax: +1-805-893-3146.
E-mail address: dennison@geog.ucsb.edu (P.E. Dennison).

0034-4257/$ - see front matter
doi:10.1016/j.rse.2003.07.001

photosynthetic vegetation (NPV) fraction from AVIRIS data to examine seasonal changes in different vegetation types present at Jasper Ridge. Green vegetation fraction and equivalent liquid water thickness declined, while NPV fraction increased in a three-date hyperspectral time series stretching from late spring to fall. Merton (1998) demonstrated seasonal changes in the shape of the red edge, quantified using the red-edge vegetation stress index (RVSI), in a five-image AVIRIS time series of Jasper Ridge. Garcia and Ustin (2001) found that mean green vegetation fraction and NPV fraction derived from AVIRIS data did not change significantly between two spring dates 1 year apart, although changes in fractions were significant at the pixel scale.

With the advent of spaceborne hyperspectral remote sensing (e.g., EO-1 Hyperion), hyperspectral monitoring of vegetation phenology should become possible in a large number of ecosystems. This paper presents a new hyperspectral time series that is used to explore the impact of seasonal changes in vegetation spectra on species-level vegetation mapping of southern California chaparral.

2. Background

Spectral mixture analysis (SMA) models image spectra as the linear combination of "pure" spectra called endmembers (Adams, Smith, & Gillespie, 1993). Endmembers can be measured in the laboratory or field or can be extracted from imagery. In SMA, a spectrum within the instantaneous field of view (IFOV) is modeled by the sum of the reflectance of each material within the IFOV multiplied by its fractional cover:

$$\rho'_\lambda = \sum_{i=1}^{N} f_i \times \rho_{i\lambda} + \varepsilon_\lambda \tag{1}$$

where $\rho_{i\lambda}$ is the reflectance of endmember i for a specific band (λ), f_i is the fraction of the endmember, N is the number of endmembers, and ε_λ is the residual error. The modeled fractions of the endmembers are typically constrained by

$$\sum_{i=1}^{N} f_i = 1 \tag{2}$$

Model fit is assessed using the model residuals (ε_λ) or the root mean square error (RMSE):

$$\mathrm{RMSE} = \sqrt{\frac{\sum_{\lambda=1}^{M} (\varepsilon_\lambda)^2}{M}} \tag{3}$$

where M is the number of bands. SMA typically assumes single interactions between photons and surfaces, producing linear mixing of the surface fractions and their reflectances. Nonlinear mixing due to multiple scattering by vegetation canopies or vegetation and soil surfaces can become significant (Borel & Gerstl, 1994; Huete, 1986; Ray & Murray, 1996; Roberts et al., 1993), and the inability to account for nonlinear mixing is an acknowledged limitation of SMA (Adams et al., 1993).

The endmembers used in SMA are uniform, regardless of whether the materials represented by the endmembers are present in all parts of the modeled image. Uncommon materials may not be represented by the set of endmembers and may be poorly modeled by SMA. SMA also does not account for spectral variation within the same material, since it permits only one endmember per material. Multiple endmember SMA (MESMA) addresses these concerns by allowing endmembers to vary on a per-pixel basis (Roberts et al., 1998). endmembers are selected from a regionally specific spectral library, which can contain image and/or reference spectra (Roberts, Dennison, Ustin, Reith, & Morais, 1999). Model fit is determined by three criteria: fraction, RMSE, and contiguous residuals (Roberts et al., 1998). The minimum RMSE model is assigned to each pixel and can be used to map materials and fractions within the image (Painter, Roberts, Green, & Dozier, 1998). Since the number of possible materials in an image can be very large, and since MESMA permits multiple endmembers for each material, an appropriate spectral library can contain hundreds of spectra. Modeling a large number of spectra for each pixel reduces the computational efficiency of MESMA and complicates interpretation of the resulting image, however. Endmember selection is necessary to create a balance between the inclusiveness of the spectral library and computational efficiency (Okin, Roberts, Murray, & Okin, 2001).

MESMA has been used to map vegetation species in southern California chaparral in the Santa Monica Mountains (Roberts et al., 1998) and in the Santa Barbara Front Range, California (Dennison & Roberts, 2003; Roberts et al., 2003). Dennison and Roberts (2003) introduced a technique for selecting endmembers for MESMA using the endmembers that best model their class within a spectral library. Each spectrum in a spectral library can be modeled by any other spectrum within the library and shade using a two endmember model. Each of these models has a goodness of fit as measured by the RMSE. endmember average RMSE (EAR) is the average RMSE for an endmember modeling the library spectra within its own material class. EAR is calculated as

$$\mathrm{EAR}_{A_i,B} = \frac{\sum_{j=1}^{n} \mathrm{RMSE}_{A_i,B_j}}{n-1} \tag{4}$$

where A is the endmember class, A_i is the endmember, B is the modeled spectra class, and n is the number of modeled spectra in class B. The "$n-1$" term accounts for the endmember modeling itself. As an example, consider spectra belonging to an "oak" class within a spectral library. Each spectrum in the oak class is treated as an endmember used to model its class. The EAR for spectrum "oak001" would be the average RMSE of a two endmember model consisting of "oak001" and shade modeling all of the spectra within the oak class. EAR is calculated for each oak spectrum as the average RMSE of each spectrum modeling all the spectra in the oak class. The endmember with the minimum EAR within a class is selected as the most representative endmember for the class.

This paper uses EAR-selected endmembers to model a time series of AVIRIS data covering a wide range of moisture availability. An enhanced version of EAR is introduced that allows for the selection of more than one endmember for each land cover class. The effectiveness of the EAR-selected endmembers for modeling image spectra is shown to be dependent on the seasonal variability of the image spectra in the time series.

3. Methods

Vegetation and impervious surfaces were mapped for the south-facing slope of the Santa Ynez Mountains and the city of Santa Barbara, CA, USA (Fig. 1). The elevation within the study area ranges from sea level at the Pacific Ocean to over 1100 m at the crest of the Santa Ynez Mountains. Natural vegetation cover on the south-facing slope of the Santa Ynez Mountains consists of schlerophyllous evergreen chaparral, dominated by *Ceanothus megacarpus* (big pod ceanothus), *Adenostoma fasciculatum* (chamise), and *Quercus agrifolia* (coast live oak). Evergreen *Arctostaphylos glandulosa* (eastwood manzanita), *Arctostaphylos glauca* (bigberry manzanita), *Ceanothus spinosus* (greenbark ceanothus), and annual and perennial introduced European grasses are locally abundant. Five vegetation land cover classes were chosen for mapping using MESMA: *C. megacarpus*, *A. fasciculatum*, *Q. agrifolia*, *Arctostaphylos* spp., and grassland. *C. spinosus* was determined to dominate primarily at a scale less than 20 m and was not mapped. The two species of *Arctostaphylos* dominant in the Santa Ynez Mountains are typically intermixed but seldom individually dominant at a resolution of 20 m, so the two *Arctostaphylos* species were combined into a single land cover type. A sixth class, impervious surface, was also mapped to evaluate the ability of EAR-selected endmembers to model a nonvegetated land cover class.

AVIRIS data were acquired on five dates over the study area. AVIRIS is a 224-band imaging spectrometer that covers a spectral range from 400 to 2500 nm (Green et al., 1998). The instrument was flown on the high-altitude ER-2 platform, producing an image swath width of approximately 11 km and IFOV of approximately 20 m. AVIRIS data were acquired in the months of May, June, and September between 1998 and 2002 (Table 1). The solar zenith angles ranged from 11.2° for the June 14, 2001 acquisition to 37.0° for the September 16, 2000 acquisition

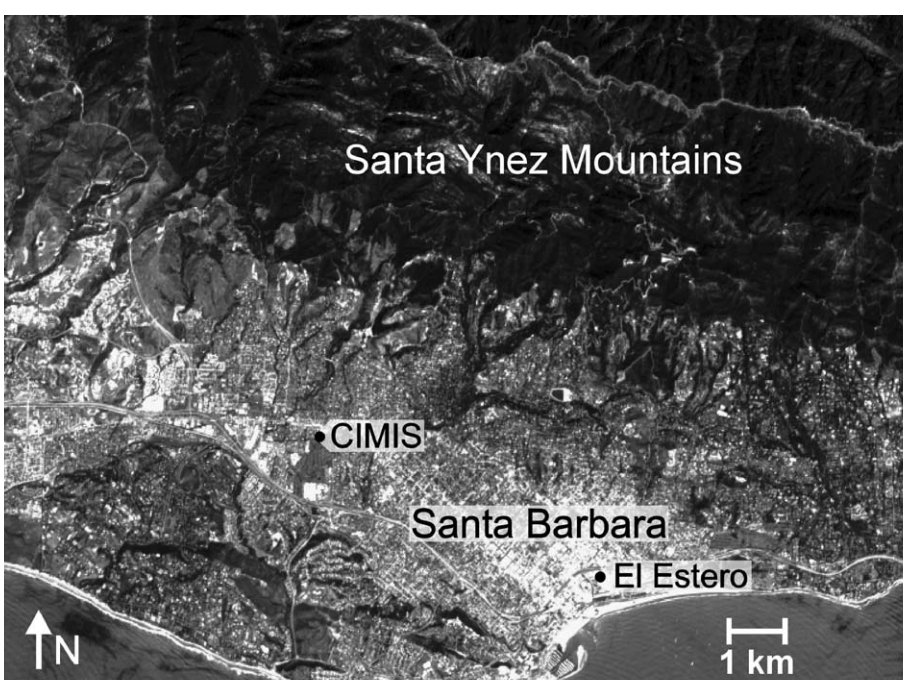

Fig. 1. The study area surrounding Santa Barbara, CA. The city of Santa Barbara covers the southern half of the study area. The northern half of the study area is the south-facing slope of the Santa Ynez Mountain range. The locations of the El Estero Water Treatment Plant and the Santa Barbara CIMIS station are shown above.

Table 1
Dates of AVIRIS data, solar zenith, and soil water balance

AVIRIS Dates	Solar zenith (°)	Soil water balance (cm)
May 30, 1998	12.5	+ 66.2
June 14, 2001	11.2	+ 12.5
May 5, 2002	19.7	− 18.4
September 16, 2000	37.0	− 37.9
September 11, 1999	32.9	− 64.0

Dates are ordered by soil water balance from positive to negative.

(Table 1). The at-sensor radiance data for all five dates were processed to apparent surface reflectance using a modified version of the MODTRAN radiative transfer model (Green, Conel, & Roberts, 1993). MODTRAN3 (Kneizys, Shettle, & Abreu, 1988) was used to generate lookup tables for path radiance and two-way transmitted solar radiance for a range of water vapor and liquid water values. The mid-latitude summer atmospheric model and multiple scattering mode were used. Modeled radiance was fit to AVIRIS-measured radiance using nonlinear least squares. A visibility of 30 km was empirically found to produce the most accurate path radiance for all five AVIRIS images. A digital elevation model was not used to correct for elevational effects. Reflectance was calibrated using the field measured reflectance spectrum of a sand target present in all five AVIRIS images.

Each reflectance image was registered to an orthorectified SPOT mosaic projected to Universal Transverse Mercator (UTM; zone 11; North American Datum 1983). The five images were transformed using triangulation and resampled to a 20-m spatial resolution using nearest neighbor resampling. The registration accuracy was estimated to be within one pixel for each image, creating a possible combined offset error of up to two pixels for any two image dates. The spatial extents of the georeferenced images are slightly different due to discrepancies in the spatial coverage of the unreferenced images and the positions of the registration points within each image.

Santa Barbara has a Mediterranean climate with a mean annual precipitation (1960–2002) of 48 cm, all in the form of rain. The timing and amount of this precipitation varies from year to year, making the date an unreliable indicator of vegetation water stress. Since the data span 5 separate years and could not be phenologically ordered by date, a simple soil water balance model was used to determine the relative moisture status for each of the five AVIRIS images. This model balanced precipitation and evapotranspiration, but neglected runoff and soil infiltration, which are more difficult to quantify. Precipitation was measured by the City of Santa Barbara Public Works Department using a rain gauge at the El Estero Water Treatment Plant in Santa Barbara (Fig. 1). Reference evapotranspiration (ET_0) was calculated from meteorological data measured at a California Irrigation Management Information System (CIMIS) station approximately 5 km to the northwest of the precipitation measurements (Fig. 1). The elevation of the precipitation station is approximately 20 m, and the elevation of the CIMIS station is approximately 60 m. ET_0 was calculated using solar irradiance, air temperature, vapor pressure, and wind speed measured over a flat, irrigated grass field using a modified Penman equation (Snyder & Pruitt, 1992). Actual evapotranspiration for natural vegetation in the Santa Ynez Mountains is lower than the ET_0 estimated for an irrigated grass field. Neglect of runoff and infiltration, differences between reference and actual evapotranspiration, and differences between the two sites in elevation and distance from the Pacific Ocean may have influenced estimated soil water balance. However, since the purpose of the model is only to measure the relative moisture status of the five AVIRIS scenes, any errors introduced by these factors are likely to be minor.

Soil water balance was calculated by cumulatively summing the daily ET_0 subtracted from the daily precipitation. Starting at the beginning of the water year (September 1), the water balance was constrained to be positive until the end of the wet season, which was determined to be the last date in the water year on which the water balance was greater than zero. Late rains in May and June of 1999, which totaled less than 3 mm of rain spread over 2 weeks, were not included in the determination of the end of the wet season for the September 11, 1999 AVIRIS image. Soil water balance was calculated for each AVIRIS image as a positive or negative value for the date the image was acquired (Table 1). Soil water balance for the five AVIRIS dates ranged from − 64.0 to + 66.2 cm. May 30, 1998 had the highest positive water balance, due to extremely high precipitation during the previous winter associated with the strong 1997–1998 El Niño. June 14, 2001 had a higher soil water balance than May 5, 2002. This reflects the timing of the end of the wet season, which lasted longer in 2001 than in 2002. The lowest negative soil water balances were the two September dates: September 11, 1999 and September 16, 2000.

Endmembers were selected for the six land cover classes from image spectra extracted from a set of reference polygons. Sixty-five vegetation reference polygons were mapped in June 2002 using field assessed vegetation cover and 1-m resolution United States Geological Survey Digital Orthophoto Quadrangles (DOQs). Ten impervious surface reference polygons were mapped in January 2003 using the DOQs. Polygons were required to be at least 40 × 40 m in size and dominated by a single land cover type (Dennison & Roberts, 2003). For each polygon, land cover dominance was categorized based on percent cover into one of six classes: 0–10%, 10–25%, 25–50%, 50–75%, 75–90%, and 90–100%. A spectral library was constructed for each AVIRIS acquisition date using the extracted image spectra from the registered AVIRIS images. Image spectra were extracted from 59 reference polygons that were >75% dominated by a single land cover class. Only image pixels that were entirely inside polygons were included in the spectral library to avoid spectral mixing of the dominant land cover type with land cover types outside the reference polygon. A total of 988 image spectra were included in the spectral library constructed for each AVIRIS image (Table 2).

EAR was calculated for each spectrum in the five spectral libraries. Two distinct variants of EAR were calculated. Single EAR, which models a class using a single two endmember model, was calculated using Eq. (4). In addition to the single EAR, a dual EAR, which models a class using the combined minimum RMSE of two 2 endmember models, was calculated using

$$\mathrm{EAR}_{A_1A_2,B} = \frac{\sum_{j=1}^{n} \min(\mathrm{RMSE}_{A_1,B_j}, \mathrm{RMSE}_{A_2,B_j})}{n-2} \tag{5}$$

where A_1 is the first endmember, and A_2 is the second endmember. The "$n-2$" term accounts for endmembers A_1 and A_2 modeling themselves. Non-shade fraction was constrained to below 106% for both the single and dual EAR calculations (Dennison & Roberts, 2003). Photometric shade was used as the shade endmember. The 106% fractional constraint was empirically determined to optimize vegetation class mapping accuracy using similar techniques on hyperspectral data of Yellowstone National Park (Halligan, 2002). For best-fit models with land cover endmember fractions above 106%, RMSE was calculated using an endmember fraction of 106% (Dennison & Roberts, 2003). The endmember with the minimum single EAR (Eq. (4)) is the single endmember with the lowest error for modeling its class. The minimum dual EAR is the pair of endmembers that together produce the lowest error for modeling their own class.

The minimum single and dual EAR endmembers were selected from the spectral library for each AVIRIS date. These endmembers were used in multiple two endmember models (each selected endmember and photometric shade constitutes a model) to map their corresponding AVIRIS images using MESMA. Non-shade fractions were constrained to between −6% and 106%, and residuals were not permitted to exceed 2.5% reflectance for more than seven contiguous bands (Dennison & Roberts, 2003; Roberts et al., 1998). RMSE was constrained below 2.5% reflectance. The model with the lowest RMSE for each image spectrum was assigned the land cover class of that endmember model. For the single EAR case, a total of six endmembers (one for each land cover type) were used to model each AVIRIS image (Table 2). Based on the accuracy of the maps produced from the minimum single EAR endmembers, minimum dual EAR endmembers were added to the library used to model the AVIRIS images. A total of 10 endmembers were used to model each AVIRIS image in the combined single and dual EAR case (Table 2).

Table 2
The number of image spectra in each land cover class for each AVIRIS acquisition date, and the number of single EAR endmembers and combined single and dual EAR endmembers for each AVIRIS date

Class	Number of image spectra	Number of endmembers, single EAR case	Number of endmembers, combined single and dual EAR case
Adenostoma fasciculatum	76	1	2
Arctostaphylos	111	1	1
Ceanothus megacarpus	398	1	2
Grassland	117	1	2
Quercus agrifolia	107	1	1
Impervious	179	1	2
Total for each image	988	6	10

4. Results

4.1. endmember selection and image modeling

The selected minimum single EAR endmembers displayed significant spectral changes over the range of soil water balance covered by the AVIRIS time series (Fig. 2). The brightness values of the selected endmember spectra for all land cover classes reflect changes in solar zenith. The 1998 and 2001 images had the lowest solar zenith angles and consistently possessed the highest reflectance endmembers of the time series. Similarly, the 1999 and 2000 images had the highest solar zeniths and the lowest reflectance endmembers. All of the vegetation endmembers selected from soil water surplus images had a distinct red edge, chlorophyll absorption in the visible wavelengths, and decreased reflectance in the shortwave infrared (SWIR) due to water absorption. Grassland endmembers exhibited the greatest changes in spectral shape over the time series (Fig. 2d). The red edge and SWIR water absorption exhibited by the grassland endmember selected from the 1998 image were greatly reduced in the 2001 and 2002 endmembers and were largely absent from the 1999 and 2000 endmembers. These changes were due to the increasing senescence of grasslands as soil water balance decreased. A red edge was apparent in all of the selected impervious surface spectra (Fig. 2f), indicating subpixel-scale vegetation was present in the urban environment. The most interesting spectral changes occurred in *A. fasciculatum*, *Arctostaphylos*, and *C. megacarpus* (Fig. 2a–c). As soil water balance decreased, the presence of NPV became more pronounced in the spectra of these endmembers. Water surplus spectra in these three land cover classes showed pronounced chlorophyll absorption at 680 nm and low ligno-cellulose absorption at 2060 and 2270 nm, while water deficit spectra showed increased ligno-cellulose absorption and decreased chlorophyll absorption. This trend was less apparent in the selected *Q. agrifolia* spectra (Fig. 2e).

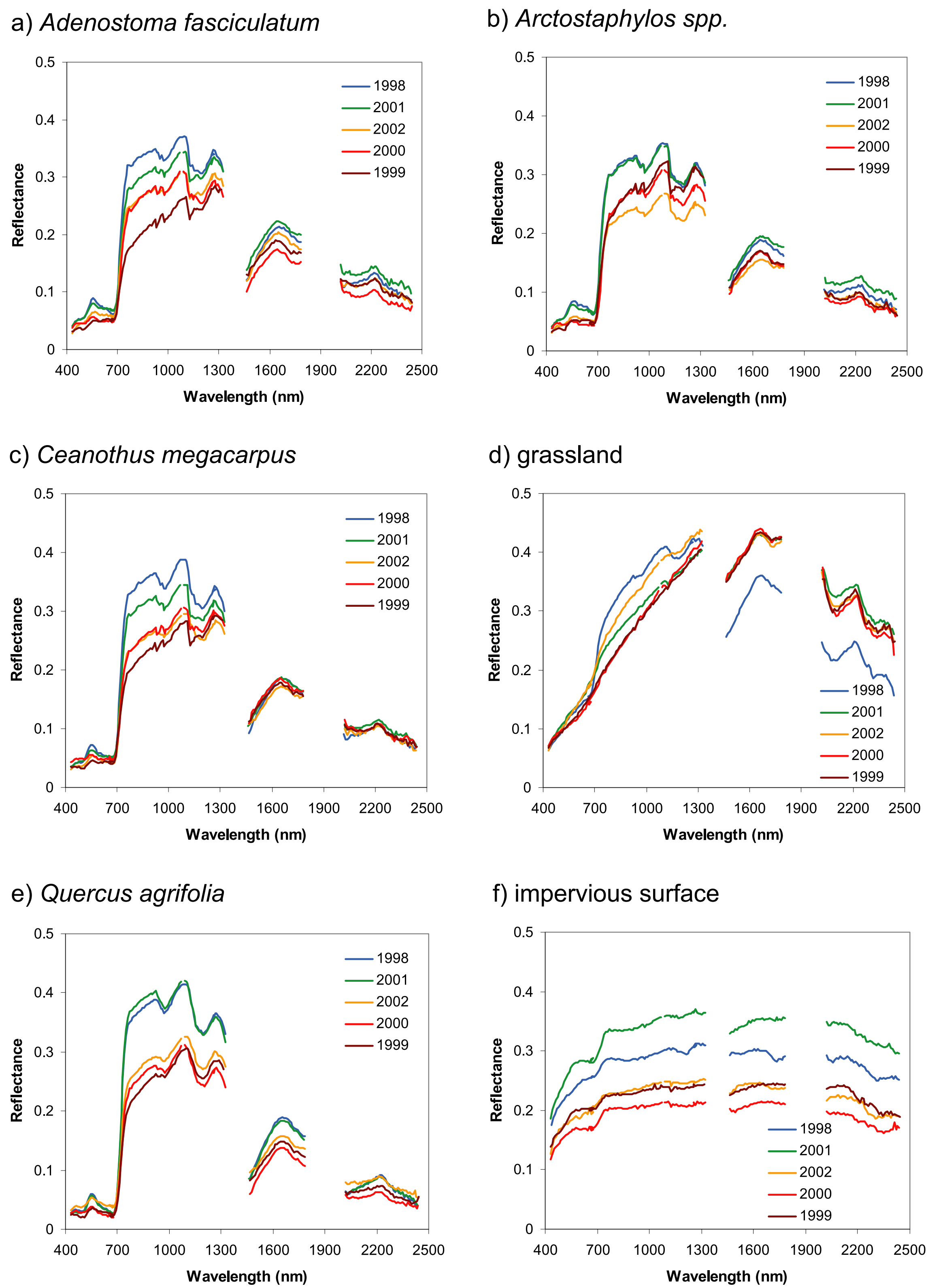

Fig. 2. The selected single minimum EAR endmembers for each land cover class, by year.

Large areas corresponding to mixed residential and riparian areas were unmodeled by the selected single EAR endmembers for all dates (Fig. 3). Neither type of unmodeled land cover was spectrally similar to the six land cover classes mapped, and the high spectral variability and spatial heterogeneity of residential neighborhoods made them dif-

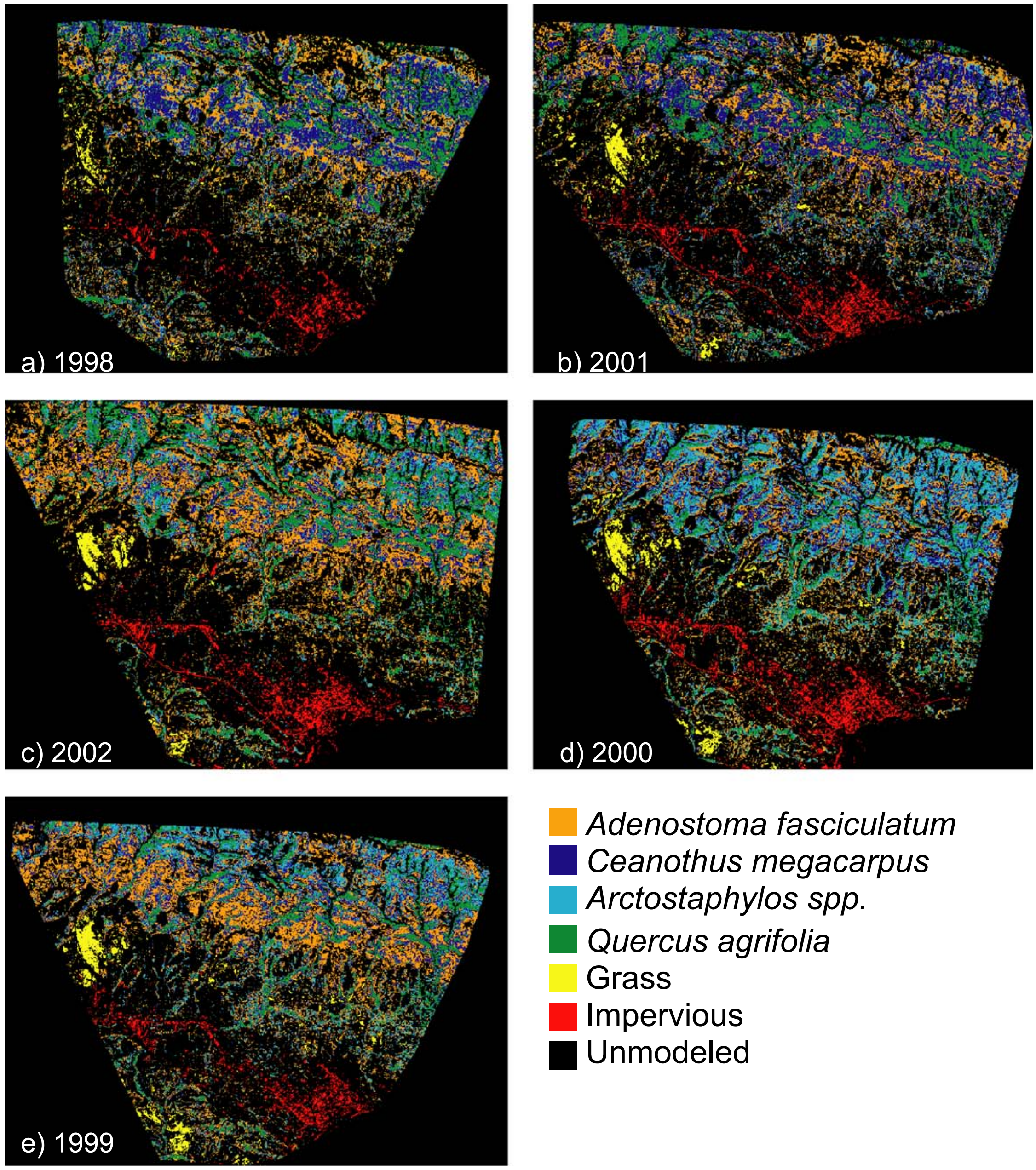

Fig. 3. AVIRIS images of the Santa Barbara front range modeled using the set of single minimum EAR endmembers for each date. Image letters correspond to the following dates: (a) May 30, 1998; (b) June 14, 2001; (c) May 5, 2002; (d) September 16, 2000; and (e) September 11, 1999.

ficult to model with only two endmembers. An average of 54.7% of the land area of the five AVIRIS images was unmodeled by the single EAR endmembers. The greatest proportion of this unmodeled area was mixed residential land cover. Urban environments possess high spectral variability and spatial heterogeneity that make them difficult to map at a resolution of 20 m (Small, 2001). When urban areas were masked out of the AVIRIS images, the average unmodeled percentage of land area declined to 35.8%.

Vegetation appears to have been well mapped in the two images with soil water surplus (Fig. 3a and b). *C. megacarpus* dominates the south-facing slope of the Santa Ynez Mountains, with bands of *A. fasciculatum* on rockier soils and *Q. agrifolia* on more mesic slopes and valley bottoms. *Arctostaphylos* spp. was properly limited to higher altitude, rocky soils. Grassland was undermodeled in the 1998 image (Fig. 3a), most likely due to varying degrees of grassland senescence. Vegetation was poorly mapped in the images with soil water deficits (Fig. 3c–e). *C. megacarpus* was undermodeled in all three water deficit images. *A. fasciculatum* was overmodeled in 1999 and 2002, while *Arctostaphylos* was overmodeled in 1999, 2000, and 2002. *Q. agrifolia* was overmodeled in the 2002 image, but appears to have been adequately modeled in the 1999 and 2000 images. Grasslands were well mapped in the two images with the largest soil water deficits: 1999 and 2000 (Fig. 3d and e). These two images were both acquired in September and contain no natural unsenesced grass. Grasslands in varying degrees of senescence in the 1998, 2001, and 2002 images increased spectral variability, leading to poorer modeling of grasslands by the selected grassland endmembers. Impervious surfaces were well mapped in the 2000, 2001, and 2002 AVIRIS images. The Santa Barbara urban core is evident in all five modeled images, but the extent of impervious surfaces, especially road surfaces, was not well mapped by the selected endmembers in the 1998 and 1999 images (Fig. 3a and e).

Dual endmembers were selected for four land cover classes (Table 2). Single endmembers selected for the grassland and impervious surface classes failed to map areas that belonged to their land cover class due to high within-class spectral variability. Using two endmembers to model each class allows for grassland endmembers with different fractions of senesced material or impervious surface endmembers with different fractions of green vegetation. Dual endmembers were also selected for *A. fasciculatum* and *C. megacarpus*. Both of these land cover classes were poorly modeled by single endmembers in the soil water deficit images. *C. megacarpus* was often modeled by *A. fasciculatum* and *Arctostaphylos* endmembers, while *A. fasciculatum* was often modeled by *Arctostaphylos* and *C. megacarpus* endmembers. Dual endmembers were not selected for *Arctostaphylos* spp. and *Q. agrifolia*. While these classes were sometimes overmapped, they did model the correct land cover class where it occurred.

The selected dual endmembers also demonstrated brightness effects due to differences in the solar zenith angle. Spectral variations in the vegetation dual endmembers showed definitive differences in NPV content between each of the two selected endmembers for each class (Fig. 4). This figure shows the dual endmember spectra selected for the 2002 AVIRIS image. The name of each spectrum includes the two-digit year of the image the spectrum was extracted from, the land cover type of the polygon the spectrum was

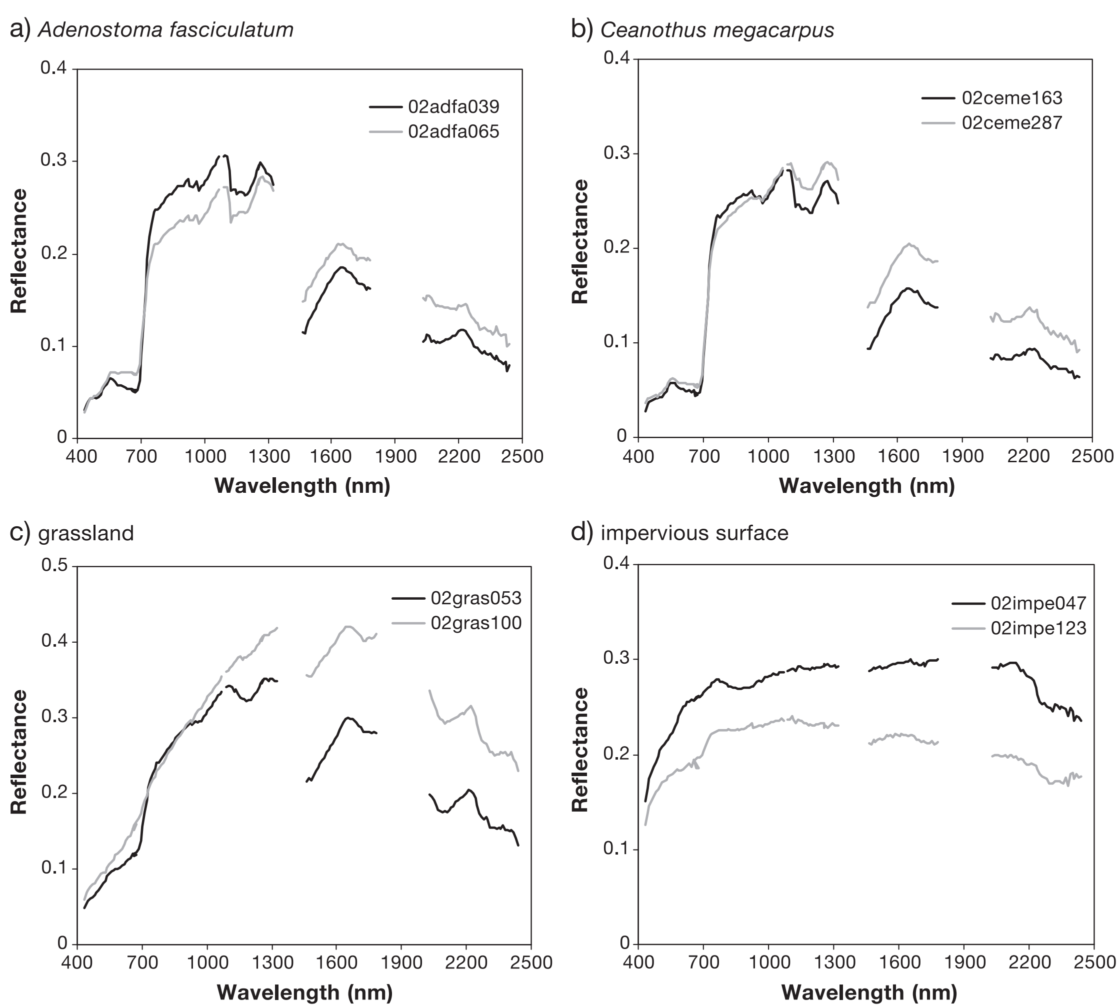

Fig. 4. Selected May 5, 2002 dual minimum EAR endmembers for *A. fasciculatum*, *C. megacarpus*, grassland, and impervious surface land cover classes. The name of each spectrum denotes the year of the image, the land cover type, and the identification number of the spectrum.

extracted from, and the identification number of the spectrum. Spectrum "02adfa065" exhibited weaker chlorophyll absorption in the visible and increased reflectance in the SWIR compared to spectrum "02adfa039" (Fig. 4a). These spectral features are consistent with higher NPV content. Similarly, "02ceme287" had higher apparent NPV content than "02ceme163" (Fig. 4b). The largest differences between dual endmembers were seen in grassland (Fig. 4c). While spectrum "02gras053" exhibited a red edge, strong water absorption bands at 970 and 1200 nm, and decreased SWIR reflectance, spectrum "02gras100" showed little red edge, weak water absorption bands, and a higher SWIR reflectance. The spectral shape of "02gras100" is consistent with fully senesced grass, while "02gras053" has a more pronounced red edge and water absorption characteristic of greener vegetation. Grasslands in the May 4, 2002 scene showed varying degrees of senescence, and the selected dual endmembers captured both green grass and senesced grass. The impervious surface dual endmembers showed a large brightness difference (Fig. 4d). Spectrum "02impe123" had a small red edge and decreased SWIR reflectance, while spectrum "02impe047" possessed a peak in reflectance in

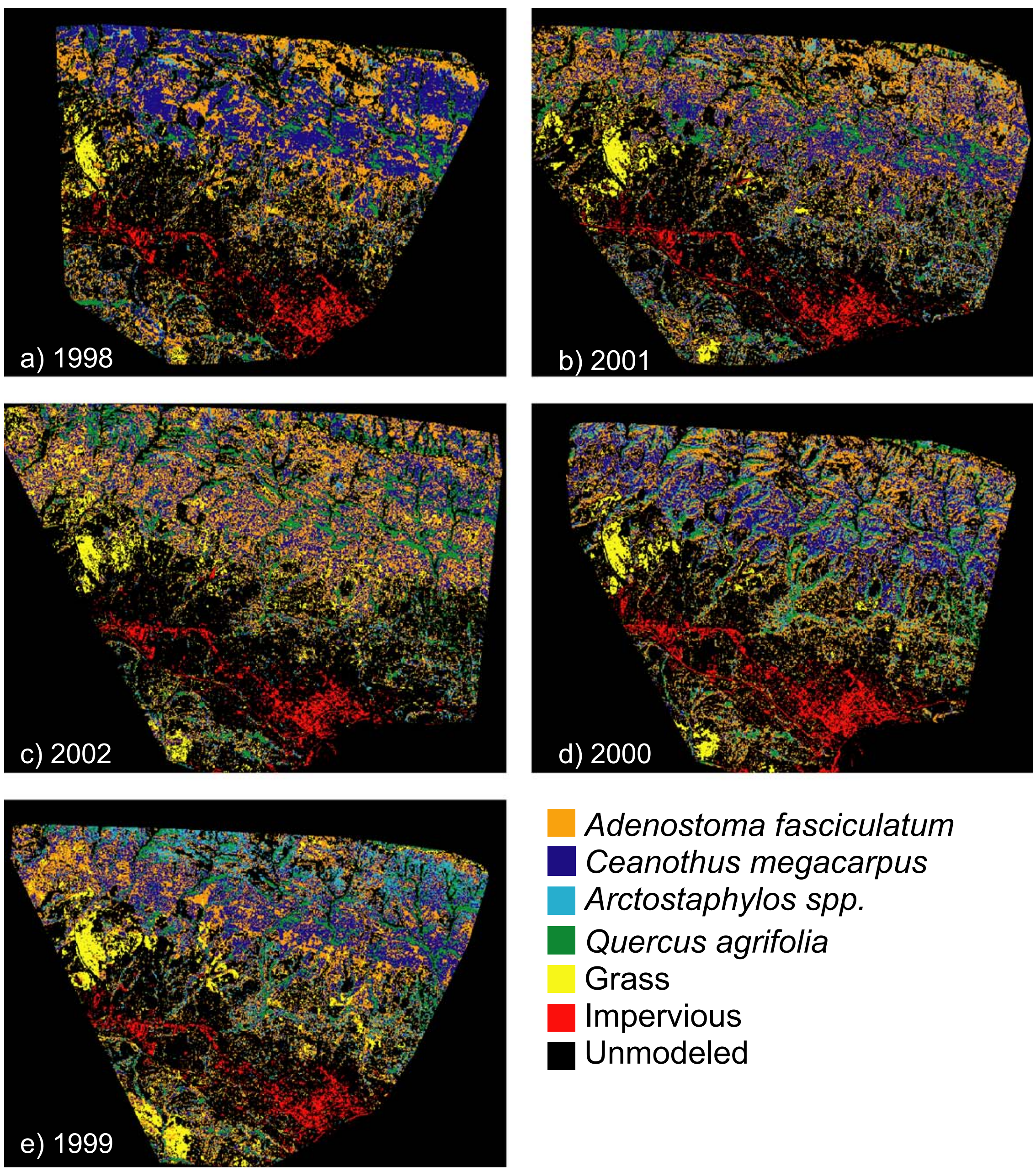

Fig. 5. AVIRIS images of the Santa Barbara front range modeled using the set of combined single and dual minimum EAR endmembers for each date. Image letters correspond to the following dates: (a) May 30, 1998; (b) June 14, 2001; (c) May 5, 2002; (d) September 16, 2000; and (e) September 11, 1999.

the near infrared that may be associated with the red edge and increased reflectance in the SWIR.

Using dual endmembers reduced the percentage of unmodeled image spectra (Fig. 5). An average of 46.5% of the land area mapped in the AVIRIS images was unmodeled by the combined single (*Arctostaphylos* and *Q. agrifolia*) and dual (*A. fasciculatum*, *C. megacarpus*, grassland, and impervious surface) EAR endmembers. As in the single EAR endmember case, the majority of the unmodeled area was mixed residential land cover. When urban areas were masked out, the average unmodeled percentage of land area declined to 26.4%. Grassland modeling improved in the 2002 image with the addition of dual grassland endmembers (Fig. 5c). Beyond an increase in the modeled area,

Table 3
Polygon dominant land cover class confusion matrices for AVIRIS images modeled using the set of single EAR endmembers

1998	Reference Dominant							
	A. fasc.	*Arcto.*	*C. mega*	grass	*Q. agri.*	imp	unmod	user's
Image Dominant *A. fasc.*	7	2	1	0	0	0	0	0.70
Arcto.	0	4	0	0	0	0	0	1.00
C. mega.	0	0	16	0	0	0	0	1.00
grass	0	0	0	4	0	0	0	1.00
Q. agri.	0	0	5	0	7	0	0	0.58
imp	0	0	0	0	0	2	0	1.00
unmod	5	0	0	7	1	7	0	0.00
producer's	0.58	0.67	0.73	0.36	0.88	0.22	–	

2001	Reference Dominant							
	A. fasc.	*Arcto.*	*C. mega*	grass	*Q. agri.*	imp	unmod	user's
Image Dominant *A. fasc.*	7	1	1	0	0	0	0	0.78
Arcto.	0	3	0	0	0	0	0	1.00
C. mega.	1	1	21	0	0	0	0	0.91
grass	0	0	0	7	0	0	0	1.00
Q. agri.	0	0	3	0	8	0	0	0.73
imp	0	0	0	0	0	4	0	1.00
unmod	4	1	0	4	0	3	0	0.00
producer's	0.58	0.50	0.84	0.64	1.00	0.57	–	

2002	Reference Dominant							
	A. fasc.	*Arcto.*	*C. mega*	grass	*Q. agri.*	imp	unmod	user's
Image Dominant *A. fasc.*	5	2	6	0	0	0	0	0.38
Arcto.	0	3	2	0	0	0	0	0.60
C. mega.	2	0	6	0	0	0	0	0.75
grass	0	0	0	7	0	0	0	1.00
Q. agri.	1	0	6	0	8	0	0	0.53
imp	0	0	0	0	0	5	0	1.00
unmod	5	1	2	4	0	4	0	0.00
producer's	0.38	0.50	0.27	0.64	1.00	0.56	–	

2000	Reference Dominant							
	A. fasc.	*Arcto.*	*C. mega*	grass	*Q. agri.*	imp	unmod	user's
Image Dominant *A. fasc.*	4	1	4	0	0	0	0	0.44
Arcto.	4	6	9	0	0	0	0	0.32
C. mega.	2	0	8	0	0	0	0	0.80
grass	0	0	0	9	0	0	0	1.00
Q. agri.	0	0	1	0	8	0	0	0.89
imp	0	0	0	0	0	4	0	1.00
unmod	4	0	2	2	0	4	0	0.00
producer's	0.29	0.86	0.33	0.82	1.00	0.50	–	

1999	Reference Dominant							
	A. fasc.	*Arcto.*	*C. mega*	grass	*Q. agri.*	imp	unmod	user's
Image Dominant *A. fasc.*	4	0	11	0	0	0	0	0.27
Arcto.	1	6	0	0	0	0	0	0.86
C. mega.	0	0	11	0	0	0	0	1.00
grass	0	0	0	9	0	0	0	1.00
Q. agri.	1	0	1	0	8	0	0	0.80
imp	0	0	0	0	0	2	0	1.00
unmod	5	0	0	2	0	7	0	0.00
producer's	0.36	1.00	0.48	0.82	1.00	0.22	–	

the soil water surplus modeled images showed little change in the distribution of mapped vegetation classes (Fig. 5a and b). The three soil water deficit images demonstrated increased modeling of *C. megacarpus* and decreased overmodeling of *Arctostaphylos* and *A. fasciculatum* (Fig. 5c–e). Some confusion between these vegetation classes still occurred in the soil water deficit images, especially in the 2002 image (Fig. 5c). The area mapped by impervious surface endmembers increased in all five images. Road surfaces that were poorly mapped by a single impervious surface endmember in 1998 and 1999 (Fig. 3a and e) were better modeled using dual impervious surface endmembers (Fig. 5a and e).

4.2. Accuracy assessment

The accuracy of the modeled images was assessed using the entire set of 75 reference polygons. Land cover class accuracy was assessed by grouping all of the modeled image spectra within a reference polygon and selecting the most frequently modeled class as the dominant class for that polygon. Polygons with equally dominant land cover classes were excluded from the accuracy assessment. User's accuracies, representing errors of commission, and producer's accuracies, representing errors of omission, were calculated for each land cover class. The confusion matrices for the single EAR-modeled images showed up to seven unmodeled polygons for grassland and impervious surface land cover classes and up to five unmodeled polygons for the *A. fasciculatum* land cover class (Table 3). *C. megacarpus* was dominant in 79% of the *C. megacarpus* polygons in the water surplus images (1998 and 2001), but was dominant in only 36% of the *C. megacarpus* polygons in the water deficit images (1999, 2000, and 2002). In the water deficit images, *C. megacarpus* polygons were modeled by the *A. fasciculatum*, *Arctostaphylos*, and *Q. agrifolia* endmembers. *A. fasciculatum* was dominant in the 58% of *A. fasciculatum* polygons in the water surplus images. In the water deficit images, *A. fasciculatum* polygons were frequently modeled by *Arctostaphylos* and *C. megacarpus* endmembers, with the correct dominance assigned for only 34% of polygons. User's accuracies were highest for grassland and impervious surface polygons, with user's accuracies of 100% for all five images.

Overall accuracy, kappa coefficient, and kappa variance were calculated for each date (Table 4) (Cohen, 1960; Congalton, 1991). These accuracy metrics were calculated both including and excluding unmodeled spectra, to separate decreased accuracy due to unmodeled polygons from decreased accuracy due to incorrectly modeled polygons. Overall accuracy was highest for the June 14, 2001 image, with an accuracy of 72% including unmodeled spectra and 90% excluding unmodeled spectra. The accuracy including unmodeled spectra of the May 30, 1998 modeled image was much lower at 59%, due to a large number of unmodeled grassland and impervious surface polygons. The accuracy for this date improved to 85% when the unmodeled spectra were excluded. The lowest accuracies were found in the water deficit images (1999, 2000, and 2002). When unmodeled spectra were excluded, the accuracy and kappa values of the water surplus images were much higher than the accuracy and kappa of the water deficit images. Confusion between the land cover classes was thus much lower in the water surplus images (Fig. 3). Kappa and kappa variance were used to calculate a Z-statistic for each pair of dates to determine whether the kappa coefficients for each date were significantly different at the 95% confidence level (Congalton, 1991). Excluding the unmodeled pixels, the kappa values of the 1998 and 2001 surplus images were significantly higher than the kappa values of the 2000 and 2002 deficit images.

The confusion matrices for the combined single and dual endmember modeled images demonstrated a decrease in the number of unmodeled polygons and in the confusion between land cover classes (Table 5). The average number of unmodeled polygons per image dropped from 14.8 polygons per image for the single EAR endmember case to 5.2 polygons per image for the combined single and dual EAR endmember case. User's and producer's accuracies improved in most cases. One of the largest sources of confusion in the combined single and dual endmember case was *A. fasciculatum* begin modeled in *C. megacarpus* polygons. *A. fasciculatum* dominated 28% of *C. megacarpus* polygons in the water deficit images (1999, 2000, and 2002). Producer's accuracy declined for *Arctostaphylos*, as 50% *Arctostaphylos* polygons were modeled as *A. fasciculatum* and *C. megacarpus.* User's accuracies were 100% for five of five dates for grassland and impervious surfaces and four of five dates for *Arctostaphylos*.

Table 4
Accuracy, kappa, and, kappa variance for AVIRIS images modeled using the set of single EAR endmembers

Year	Including unmodeled spectra			Excluding unmodeled spectra		
	Accuracy	Kappa	Kappa variance	Accuracy	Kappa	Kappa variance
1998	0.80	**0.75**	0.0033	0.90	0.87	0.0022
2001	0.78	0.73	0.0036	0.89	0.86	0.0023
2002	0.68	**0.61**	0.0047	0.74	0.68	0.0045
2000	0.72	**0.66**	0.0042	0.80	0.75	0.0036
1999	0.77	**0.72**	0.0040	0.81	0.76	0.0035

Statistics are shown for both polygon dominance assessed including the unmodeled spectra and polygon dominance assessed excluding the unmodeled spectra. Shaded rows indicate water deficit images.

Table 5
Polygon dominant land cover class confusion matrices for AVIRIS images modeled using the set of combined single and dual EAR endmembers

1998 — Reference Dominant

Image Dominant	*A. fasc.*	*Arcto.*	*C. mega*	grass	*Q. agri.*	imp	unmod	user's
A. fasc.	11	2	2	0	0	0	0	0.73
Arcto.	0	3	0	0	0	0	0	1.00
C. mega.	0	2	22	0	0	0	0	0.92
grass	0	0	0	9	0	0	0	1.00
Q. agri.	0	0	1	0	7	0	0	0.88
imp	0	0	0	0	0	4	0	1.00
unmod	1	0	0	2	1	3	0	0.00
producer's	0.92	0.43	0.88	0.82	0.88	0.57	–	

2001 — Reference Dominant

Image Dominant	*A. fasc.*	*Arcto.*	*C. mega*	grass	*Q. agri.*	imp	unmod	user's
A. fasc.	8	0	4	0	0	0	0	0.67
Arcto.	1	5	0	0	0	0	0	0.83
C. mega.	1	2	19	0	0	0	0	0.86
grass	0	0	0	8	0	0	0	1.00
Q. agri.	0	0	0	0	8	0	0	1.00
imp	0	0	0	0	0	6	0	1.00
unmod	3	0	0	3	0	1	0	0.00
producer's	0.62	0.71	0.83	0.73	1.00	0.86	–	

2002 — Reference Dominant

Image Dominant	*A. fasc.*	*Arcto.*	*C. mega*	grass	*Q. agri.*	imp	unmod	user's
A. fasc.	9	3	7	0	0	0	0	0.47
Arcto.	0	2	0	0	0	0	0	1.00
C. mega.	2	2	11	0	0	0	0	0.73
grass	0	0	0	8	0	0	0	1.00
Q. agri.	0	0	3	0	8	0	0	0.73
imp	0	0	0	0	0	8	0	1.00
unmod	1	0	0	3	0	1	0	0.47
producer's	0.75	0.29	0.52	0.73	1.00	0.89	–	

2000 — Reference Dominant

Image Dominant	*A. fasc.*	*Arcto.*	*C. mega*	grass	*Q. agri.*	imp	unmod	user's
A. fasc.	8	4	6	0	0	0	0	0.44
Arcto.	0	2	0	0	0	0	0	1.00
C. mega.	2	1	16	0	0	0	0	0.84
grass	0	0	0	9	0	0	0	1.00
Q. agri.	0	0	1	0	8	0	0	0.89
imp	0	0	0	0	0	7	0	1.00
unmod	1	0	0	2	0	2	0	0.44
producer's	0.73	0.29	0.70	0.82	1.00	0.78	–	

1999 — Reference Dominant

Image Dominant	*A. fasc.*	*Arcto.*	*C. mega*	grass	*Q. agri.*	imp	unmod	user's
A. fasc.	7	1	6	0	0	0	0	0.50
Arcto.	0	5	0	0	0	0	0	1.00
C. mega.	4	0	16	0	0	0	0	0.80
grass	0	0	0	10	0	0	0	1.00
Q. agri.	1	0	2	0	8	0	0	0.73
imp	0	0	0	0	0	8	0	1.00
unmod	1	0	0	0	0	1	0	0.50
producer's	0.54	0.83	0.67	1.00	1.00	0.89	–	

Overall accuracy, kappa coefficient, and kappa variance were also calculated for the combined single and dual endmember case (Table 6). The increase in the number of modeled polygons and reduced confusion between land cover increased the overall accuracy and kappa coefficient for all five dates when unmodeled spectra were included. The increases in kappa were found to be significant at the 95% confidence level for all dates except for June 14, 2001 (Table 6). The 1998 image had the highest overall accuracies with an accuracy of 80% including unmodeled spectra and an accuracy of 90% excluding unmodeled spectra. Water surplus images (1998 and 2001) still possessed higher accuracies than the water deficit images, but the differences in accuracy between the two decreased. Excluding unmod-

Table 6
Accuracy, kappa, and kappa variance for AVIRIS images modeled using the set of combined single and dual EAR endmembers

Year	Including unmodeled spectra			Excluding unmodeled spectra		
	Accuracy	Kappa	Kappa variance	Accuracy	Kappa	Kappa variance
1998	0.80	**0.75**	0.0033	0.90	0.87	0.0022
2001	0.78	0.73	0.0036	0.89	0.86	0.0023
2002	0.68	**0.61**	0.0047	0.74	0.68	0.0045
2000	0.72	**0.66**	0.0042	0.80	0.75	0.0036
1999	0.77	**0.72**	0.0040	0.81	0.76	0.0035

Statistics are shown for both polygon dominance assessed including the unmodeled spectra and polygon dominance assessed excluding the unmodeled spectra. Shaded rows indicate water deficit images. Values in bold are significant improvements (0.95 confidence over single EAR endmember modeled images.

eled image spectra increased accuracy over the single EAR endmember case for all dates and increased kappa for all dates except for 2001 (Table 6). This indicates that the improvements in accuracy are also due to reduced confusion between land cover classes and not solely caused by the modeling of previously unmodeled image spectra.

5. Discussion

Modeling accuracy and the quality of the modeled maps were higher for the water surplus images than for the water deficit images. As the soil water balance decreases, the amount of senesced and dead material in a stand of vegetation increases. Even if the dominant species is not subject to senescence or dieback, subdominant grasses and senescent shrubs (e.g., *Saliva* spp.) growing in openings in the chaparral canopy may respond more readily to changes in soil moisture status. *A. fasciculatum* and *C. megacarpus* become less separable under drought conditions due to varying NPV content within chaparral stands. In the single EAR endmember case, greener *C. megacarpus* polygons were modeled by the selected *C. megacarpus* endmember. *C. megacarpus* polygons with higher NPV content were modeled by the *A. fasciculatum* and *Arctostaphylos* endmembers, which also display spectral features consistent with higher NPV content. Similarly, greener *A. fasciculatum* image spectra were modeled by the *C. megacarpus* endmember rather than the *A. fasciculatum* endmember with higher NPV content.

Using dual endmembers reduced the confusion between species by allowing two endmembers with different NPV content to be selected. Dual EAR endmembers for *A. fasciculatum* and *C. megacarpus* reduced confusion between these species by correctly modeling image spectra that contained a range of NPV content. Although confusion was reduced by dual EAR endmembers, water surplus images were still better modeled than water deficit images by a margin of 8–16% accuracy when unmodeled spectra were excluded. Image spectra from the water surplus images displayed smaller variations in NPV content, allowing single or dual endmembers to model land cover relatively accurately. Image spectra from the water deficit images possessed more variable NPV content, which led to confusion between vegetation classes even with dual endmembers.

An examination of the areas modeled by the dual endmembers revealed differences in the spatial distribution of vegetation water stress. Grassland endmembers with distinctly different NPV content were selected for the June 14, 2001 AVIRIS image (Fig. 6). The areas modeled by the

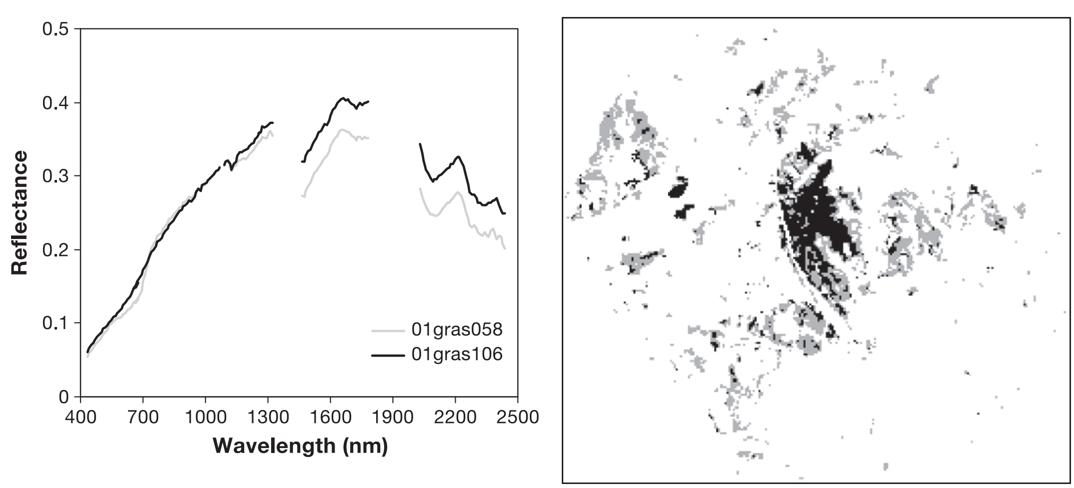

Fig. 6. Dual endmembers selected to model grassland in the 2001 AVIRIS image (left) and a subset of the areas modeled by these endmembers (right). Black pixels were modeled by 01gras106 and shade. Gray pixels were modeled by 01gras058 and shade.

endmember with higher NPV content were hilltop pastures covered by senesced grass. The more mesic slopes, which possessed greener grass than the hilltops, were modeled by the endmember with a pronounced red edge and reduced reflectance in the SWIR. Multiple endmembers containing a range of NPV fractions could be used to monitor soil water balance in each land cover class. This measurement of drought stress in each class could be further refined by using three endmember models consisting of an endmember for the vegetation type, a generic NPV endmember, and shade. The resulting NPV fraction could provide a continuous measure of drought stress for each dominant chaparral species.

The bidirectional reflectance distribution functions (BRDF) of the land cover classes and solar zenith angles may affect the portability of the selected endmembers to other locations within an image and between image dates. Due to the orientation of the AVIRIS images used in this study, each land cover class had a relatively small range of viewing zenith angles. All of the impervious surface polygons were positioned in the forward scattering portions of the five AVIRIS images. The *Q. agrifolia* polygons possessed primarily nadir viewing geometries, while the *A. fasciculatum*, *Arctostaphylos* spp., and *C. megacarpus* polygons possessed only backscattering geometries. Only grassland polygons had both forward scattering and backscattering viewing geometries. endmembers selected based on at small range of view angles may not be optimal for modeling spectra at all viewing geometries. Dual endmembers could be selected from spectra taken from a variety of viewing geometries to best model non-Lambertian materials. Solar zenith angles complicate the portability of endmembers between image dates. Land cover classes with large vertical relief, such as *Q. agrifolia* and impervious surfaces, will demonstrate the largest increase in shade fraction as the solar zenith angle increases. endmembers selected from images with lower solar zenith angles will model spectra from images with higher solar zenith angles, but the reverse conditions may violate the superpositive fraction constraint.

A major drawback of limiting MESMA to two endmembers is the large number of unmodeled image spectra. Single EAR endmembers modeled an average of 45.3% of the five AVIRIS images, while combined single and dual EAR endmembers modeled an average of 53.5% of the five AVIRIS images. The unmodeled areas of the images contain spectral mixtures that are difficult to model using two endmembers. The incorporation of three endmember models would greatly increase the modeled area (as shown by Dennison & Roberts, in press and Roberts et al., 2003) in addition to accounting for variations in NPV content. Residential areas, by far the largest unmodeled land cover type within the AVIRIS images, are a spectral mixture of impervious surfaces (e.g., roads and rooftops) and vegetation (e.g., grass and trees). Small (2001) suggests that three and four endmember models are necessary for modeling urban areas. A three endmember model containing an impervious surface endmember, a green vegetation endmember, and shade may be able to model these spectrally mixed areas. Future efforts will concentrate on expanding the EAR technique to include selection for three endmember models by combining minimum EAR two endmember models (Dennison & Roberts, 2003) or by calculating average error using a three endmember model.

6. Conclusions

In this paper, we expand EAR to select the pair of endmembers with the lowest average error to be selected from a spectral library. Single and dual EAR endmembers were selected for six land cover classes from five AVIRIS images with varying soil moisture availability. Selected endmembers demonstrated seasonal changes in spectral shape that were characteristic of increased NPV content in water deficit images. When used to model the AVIRIS images, confusion between endmembers increased as soil water balance changed from positive to negative, reducing the accuracy of the modeled water deficit images by 6–27% when unmodeled spectra were excluded. The maximum accuracy for all six land cover classes was 90%. For vegetation mapping, images with low variability in NPV content are desirable. The highest user's and producer's accuracies for four chaparral vegetation species occurred on water surplus dates, while the highest user's and producer's accuracies for the grassland class were found in full senesced conditions. Given the increased confusion between chaparral species in the images with soil water deficits, site quality is likely more important than a species' typical response to seasonal water stress for determining the NPV content of a stand of chaparral. The increase in confusion between species associated with soil water deficits has implications for mapping vegetation using broadband sensors, as well. While broadband sensors lack the spectral resolution to separate NPV and soil, data from broadband sensors such as Landsat TM/ETM+ and MODIS will still be sensitive to variability in the SWIR produced by NPV. Separating similar chaparral species using broadband data will also be most effective when images with soil water surpluses are used.

Acknowledgements

Support for this research was provided by a National Aeronautics and Space Administration (NASA) Earth Systems Science Fellowship (NGT5-50327) and the NASA Solid Earth and Natural Hazards (NAG2-1140), Regional Earth Science Application Center (CSDH NASA RESAC 447633-59075), and EO-1 Science Validation (NCC5-496) programs.

References

Adams, J. B., Smith, M. O., & Gillespie, A. R. (1993). Imaging spectroscopy: Interpretation based on spectral mixture analysis. In C. M. Pieters, & P. A. J. Englert (Eds.), *Remote geochemical analysis: Elemental and mineralogical composition* (pp. 145–166). Cambridge, UK: Press Syndicate of University of Cambridge.

Borel, C. C., & Gerstl, S. A. W. (1994). Nonlinear spectral mixing models for vegetative and soil surfaces. *Remote Sensing of Environment*, *47*, 403–416.

Cohen, J. (1960). A coefficient of agreement for nominal scales. *Educational and Psychological Measurement*, *20*, 37–46.

Congalton, R. (1991). A review of assessment the accuracy of classifications of remotely sensed data. *Remote Sensing of Environment*, *37*, 35–46.

DeFries, R., Hansen, M., & Townshend, J. (1995). Global discrimination of land cover types from metrics derived from AVHRR Pathfinder data. *Remote Sensing of Environment*, *54*, 209–222.

DeFries, R. S., & Townshend, J. R. G. (1994). NDVI-derived land cover classifications at a global scale. *International Journal of Remote Sensing*, *15*, 3567–3586.

Dennison, P. E., & Roberts, D. A. (2003). endmember selection for mapping chaparral species and fraction using Multiple endmember Spectral Mixture Analysis. *Remote Sensing of Environment*, *41*, 123–135. (doi:10.1016/S0034-4257(03)00135-4)

Elvidge, C. D., & Portigal, F. P. (1990). Change detection in vegetation using 1989 AVIRIS data. *SPIE imaging spectroscopy of the terrestrial environment* (pp. 178–189). Orlando, FL: SPIE.

Garcia, M., & Ustin, S. L. (2001). Detection of interannual vegetation responses to climatic variability using AVIRIS data in a coastal savanna in California. *IEEE Transactions on Geoscience and Remote Sensing*, *39*, 1480–1490.

Green, R., Conel, J., & Roberts, D. (1993). Estimation of aerosol optical depth and additional atmospheric parameters for the calculation of apparent surface reflectance from radiance as measured by the Airborne Visible-Infrared Imaging Spectrometer (AVIRIS). *Summaries of the Fourth Annual JPL Airborne Geosciences Workshop* (pp. 73–76). Pasadena, CA: Jet Propulsion Laboratory.

Green, R. O., Eastwood, M. L., Sarture, C. M., Chrien, T. G., Aronsson, M., Chippendale, B. J., Faust, J. A., Pavri, B. E., Chovit, C. J., Solis, M., Olah, M. R., & Williams, O. (1998). Imaging spectroscopy and the Airborne Visible/Infrared Imaging Spectrometer (AVIRIS). *Remote Sensing of Environment*, *65*, 227–248.

Halligan, K. Q. (2002). Multiple endmember spectral mixture analysis of vegetation in the northeast corner of Yellowstone national park. Master's Thesis, University of California Santa Barbara.

Hobbs, R. J. (1989). Remote sensing of spatial and temporal dynamics of vegetation. In R. J. Hobbs, & H. A. Mooney (Eds.), *Remote sensing of biosphere functioning* (pp. 203–219). New York: Springer-Verlag.

Huete, A. R. (1986). Separation of soil–plant spectral mixtures by factor analysis. *Remote Sensing of Environment*, *19*, 237–251.

Kneizys, F. X., Shettle, E. P., & Abreu, L. W. (1988). *User's guide to Lowtran 7*. Report No. AFGL-TR-88-0177, United States Air Force Geophysical Laboratory, Bedford, MA.

Lambin, E. F. (1996). Change detection at multiple temporal scales—seasonal and annual variations in landscape variables. *Photogrammetric Engineering and Remote Sensing*, *62*, 931–938.

Loveland, T. R., Reed, B. C., Brown, J. F., Ohlen, D. O., Zhu, Z., Yang, L., & Merchant, J. W. (2000). Development of a global land cover characteristics database and IGBP DISCover from 1 km AVHRR data. *International Journal of Remote Sensing*, *21*, 1303–1330.

Merton, R. N. (1998). Monitoring community hysteresis using spectral shift analysis and the red-edge vegetation stress index. *Proceedings of the Seventh JPL Airborne Earth Science Workshop* (pp. 275–284). Pasadena, CA: Jet Propulsion Laboratory.

Okin, G. S., Roberts, D. A., Murray, B., & Okin, W. J. (2001). Practical limits on hyperspectral vegetation discrimination in arid and semiarid environments. *Remote Sensing of Environment*, *77*, 212–225.

Painter, T. H., Roberts, D. A., Green, R. O., & Dozier, J. (1998). The effect of grain size on spectral mixture analysis of snow-covered area from AVIRIS data. *Remote Sensing of Environment*, *65*, 320–332.

Ray, T. W., & Murray, B. C. (1996). Nonlinear spectral mixing in desert vegetation. *Remote Sensing of Environment*, *55*, 59–64.

Roberts, D. A., Dennison, P. E., Gardner, M., Hetzel, Y. L., Ustin, S. L., & Lee, C. (2003). Evaluation of the potential of Hyperion for fire danger assessment by comparison to the Airborne Visible Infrared Imaging Spectrometer. *IEEE Transactions on Geoscience and Remote Sensing,* 41, 1297–1310.

Roberts, D. A., Dennison, P. E., Ustin, S. L., Reith, E., & Morais, M. E. (1999). Development of a regionally specific library for the Santa Monica Mountains using high resolution AVIRIS data. *Proceedings of the Eighth JPL Airborne Earth Science Workshop* (pp. 349–354). Pasadena, CA: Jet Propulsion Laboratory.

Roberts, D. A., Gardner, M., Church, R., Ustin, S., Scheer, G., & Green, R. O. (1998). Mapping chaparral in the Santa Monica Mountains using multiple endmember spectral mixture models. *Remote Sensing of Environment*, *65*, 267–279.

Roberts, D. A., Green, R. O., & Adams, J. B. (1997). Temporal and spatial patterns in vegetation and atmospheric properties from AVIRIS. *Remote Sensing of Environment*, *62*, 223–240.

Roberts, D. A., Smith, M. O., & Adams, J. B. (1993). Green vegetation nonphotosynthetic vegetation and soils in AVIRIS data. *Remote Sensing of Environment*, *44*, 255–269.

Small, C. (2001). Multiresolution analysis of urban reflectance. *Remote sensing data fusion over urban areas, IEEE/ISPRS Joint Workshop 2001* (pp. 15–19). Rome, Italy: IEEE.

Snyder, R., & Pruitt, W. (1992). Evapotranspiration data management in California. In T. Engman (Ed.), *Irrigation and drainage: Saving a threatened resource—in search of solutions* (pp. 128–133). New York: American Society of Civil Engineers.